

Full Length Article

Amyloid fibrils with charge transportation facilitating the green synthesis of single-crystalline gold nanoplates for catalytic application



Liwei Zhang^{a,1}, Peng Zhang^{b,1}, Rongrong Wu^a, Aoze Han^c, Kai Cheng^a, Zengkai Wang^a, Juan Yang^a, Shuai Hou^a, Yi Tong^c, Mingdong Dong^d, Lei Liu^{a,*}

^a Institute for Advanced Materials, School of Materials Science and Engineering, Jiangsu University, Zhenjiang 212013, China

^b Key Laboratory for Water Quality and Conservation of the Pearl River Delta, Ministry of Education, Institute of Environmental Research at Greater Bay, Guangzhou University, Guangzhou 510006, China

^c College of Integrated Circuit Science and Engineering, Nanjing University of Posts and Telecommunications, Nanjing 210023, China

^d Interdisciplinary Nanoscience Center (iNANO), Aarhus University, Aarhus C DK-8000, Denmark

ARTICLE INFO

ABSTRACT

Keywords:

Amyloid assembly
Charge transfer
Green chemistry
Gold nanoplates
Catalysts

Peptide assemblies as the significant units in biological system play the key role in various activities i.e., charge transportation and metal ion reduction, which is rarely clarified with detailed mechanism. Herein, we determined the band gap of hIAPP₂₀₋₂₉ to be about 2.5 eV by theoretical simulations, and peptides could self-assemble into amyloid fibrils. Further experiments confirmed the charge transport along the surface of amyloid fibril by setting electrical device. All the electroactive features of peptides combined with its capability of binding gold precursor and transferring electron to gold precursor would facilitate the reduction of gold ions to single-crystalline gold nanoplates. The obtained gold nanoplate-fibrils (Au-fibrils) hybrids were employed as catalysts in the reduction of 4-nitrophenol with good performances. We envision that amyloid fibrils with charge transportation inspired from the bio-system could be applied to manufacture peptide-metal nanomaterials in a green and precise manner for further catalytic applications.

1. Introduction

Biological systems such as bacteria, yeast and fungi have been considered to be eco-friendly reducing and capping agents for the green synthesis of inorganic-based hierarchical nanostructures, which have been widely applied in biology and biomaterial science, such as biosensing and bioimaging [1–5]. It is known that electron or charge transportation existing in the bio-system, and many attempts have been made to reveal the reduction mechanism of micro-organisms and the role of electron or charge transportation during the reduction, however, a clear understanding has not yet been achieved, mainly due to the complexity of biological reactions in biosystems [1,2]. Recently, biomolecules, especially proteins and peptides as the basic and simple unit compared to bacteria, were verified to have the excellent capability to mediate synthesis of metal nanostructures, e.g., nanoparticles, nanoplates and giant nanosheets, etc [6–9]. For instance, β -lactoglobulin fibrils and the natural fibrous protein silk fibroin have been explored to generate two-dimensional single-crystalline gold nanosheets, which

have been further applied in various functional applications [9–11]. The possible mechanism of protein as the reducing agent is related to the specific amino acids composing the protein [10]. In the redox process, some specific amino acids, i.e., tryptophan, tyrosine, lysine, arginine, aspartic acid and glutamic acid, are the main contributors to mediate the synthesis of single-crystalline Au microflakes or nanosheets. In recent, a tyrosine rich α -helical peptide was proposed to be a new reducing agent to construct large-scale single-crystalline two dimensional silver nanosheets with controllable morphology and crystal growth at room temperature by specifically co-assembling with metal ions [12]. So far, the general rule obtained might be that amino acids with indole and phenol groups could reduce the metal ions, e.g., AuCl_4^- and Ag^+ , due to the electron-donor property of the residues [13]. In recent, some amino acids including carboxyethyl, guanidine and amine groups, without indole or phenol groups, were also proved to be able to direct Au nanosheets or microflakes formation [14]. However, it is significant and should be clarified that the reduction is also relied on the whole peptide or peptide assemblies as the synergistic action, not only the specific

* Corresponding author.

E-mail address: liul@ujs.edu.cn (L. Liu).

¹ These authors contributed equally.

amino acids.

Actually, peptides are composed of 20 amino acids, which cooperatively contribute to specific physical (optical, electrical) and chemical (selective binding, self-assembly) functions, which played a significant role in energy or electron transfer in the biological system [15–19]. For instance, it has been illustrated that the aromatic interactions and hydrogen bonding networks in amyloid peptide nanostructure could lead to the dipole moment or formation of quantum confined domains [20–23], which endows the peptides with desired electronic properties to the construction of photonic amyloid based materials, temperature-dependent electrical conductive materials, ferroelectric materials, etc [21,24–30]. Although some proteins or peptides have exhibited the electro active property, it is not closely related to the green synthesis of reducing metal ions to nanostructures. The mechanistic insight of reduction mentioned above need to be clarified as well as the structures of protein or protein assemblies.

Herein, we selected the human islet amyloid polypeptide motif (*h*IAPP_{20–29}, without redox amino acids), the key fragment of *h*IAPP with intrinsic self-assembling capability to form nanofibrils, as the demonstration. Most importantly, we explored and proved the electroactivity of *h*IAPP_{20–29} fibrils, which was rarely examined before. We exhibited amyloid peptide assemblies as the simple model from bio-system possessing the ability of charge transportation, which is a represented feature of bio-system. All the electronical character of amyloid peptide combined with the ability of binding metal ions and making electron transfer could facilitate the reduction of metal ion to form two-dimensional single-crystalline gold nanostructures. The as-prepared Au-fibrils hybrids as the catalyst further displayed remarkable performance. The finding in this work revealed that amyloid peptide assemblies as the representative of simple model from bio-system to importantly explain how the structure and surface property can efficiently facilitate the metal ion reduction by theoretical simulation and typical memristors. This might advance the knowledge of green synthesis of metal nanostructure by modulating surface property of reducing agents. As the useful strategy, one could guide the construction of the variety of peptide-metal nanomaterials in an eco-friendly approach, which would be further applied well in catalysis, biosensing and bioimaging, etc.

2. Experimental

2.1. Reagents and chemicals

Gold (III) chloride trihydrate (HAuCl₄·3H₂O, 99.9%) was purchased from Sigma-Aldrich. Sodium hydroxide (NaOH, 96%) and sodium borohydride (NaBH₄, 98%) were purchased from Sinopharm Chemical Reagent Co., Ltd; Thioflavin T (ThT, 95%) was purchased from Ti xi'ai (Shanghai) Chemical Industry Co., Ltd; 4-nitrophenol (AR, 98%) was purchased from Shanghai Aladdin Biochemical Technology Co., Ltd. The *h*IAPP_{20–29} (SNNFGAILSS, purity > 98%) was synthesized and purified by Guoping Pharmaceutical Co., Ltd (Hefei, China). Deionized water (Milli-Q grade) with a resistivity of 18.2 MΩ was used for all solution preparation.

2.2. Synthesis and characterization of the *h*IAPP_{20–29} fibrils

*h*IAPP_{20–29} was dissolved in water at a concentration of 500 μM. The mixture was shaken vigorously to ensure fully dissolution. Subsequently, the solution was placed in a thermo-shaker (PHMT, Grant Instruments, England) at 360 rpm and 37 °C for 12 h. Finally, the polypeptide suspension was stored at 4 °C for further use. ThT fluorescence assay was employed to monitor the dynamics of *h*IAPP_{20–29} aggregation and fibrillation. The fluorescence intensity was recorded by using a Hitachi F-4500 fluorescence spectrophotometer (Japan) with excitation at 450 nm and emission at 485 nm, respectively. A total of 250 μL sample solution composed of deionized water, polypeptide solution and 1 mM ThT solution was added into a 0.1 cm quartz cell for the

measurement. The volume ratio of solvent, polypeptide and ThT solution was 8:1:1. All samples were measured three times. Circular dichroism (CD) spectra of the polypeptide solution, incubated for 0.5 h, 4 h and 12 h, were performed over the range from 190 nm to 250 nm with a scan speed of 50 nm/min and bandwidth of 2 nm on a JASCO PTC-348 W1 spectropolarimeter. The atomic force microscope (AFM) images of polypeptide fibrils incubated for 0.5 h, 4 h and 12 h, with a resolution of 512 × 512 pixel were collected on Multimode VIII SPM (Bruker, Germany) in tapping mode in a quiet room at room temperature.

2.3. Preparation of gold nanoplates

A chloroauric acid solution (50 μL, 18 mM) was mixed with 400 μL of the long fibrils solution. Then, the mixed solution was placed in a water bath for 120 h without disturbance at 25, 37 and 60 °C to obtain the Au-fibrils composite solution. Afterwards, the product was centrifuged at 2000 rpm for 5 min, and the precipitate was redissolved in a sodium hydroxide solution of pH = 12 and reacted for 12 h at 80 °C. The alkaline washing solution was centrifuged at 2000 rpm for 5 min, and the precipitate was resuspended in water each time, and the above procedure was repeated three times for further characterizations.

2.4. Characterizations of the gold nanoplates

The polypeptide fibrils and chloroauric acid solution were fully mixed and reacted at 37 °C, and the solutions at different reaction time were taken out for UV-Vis spectroscopic characterization on a UV2600i spectrometer (Shimadzu, Japan). The morphology of the gold nanoplates obtained after cleaning with sodium hydroxide solution was tested with atomic force microscope, transmission electron microscope (FEI, model CM12, NL) and scanning electron microscope (FEI, Eindhoven, NL) with energy dispersive spectroscopy elemental mapping. Selected area electron diffraction (SAED) was examined on the same TEM in the diffraction mode. X-ray photoelectron spectra (XPS) of gold nanoplates were measured on an ESCALAB 250 spectrometer (PHI5000 Versa Probe) using Al Kα radiation at 1486.6 eV. The resolution of the XPS is ± 0.1 eV. The binding energies of gold nanoplates were analyzed with respect to C 1s peak of contaminated carbon at 284.6 eV. X-ray diffraction (XRD) was applied (Rigaku D/max-rA) to identify the crystalline-phase structures of gold nanoplates.

2.5. Electrostatic force microscopy

High-temperature oriented pyrolysis graphite (HOPG) was pasted on a round iron plate by conductive adhesive. Then, the polypeptide fibrils solution was dropped onto the surface of the HOPG, and dried naturally at room temperature. Finally, all samples were imaged on the electrostatic force microscope (Multimode VIII, Bruker). We used Co/Cr coated highly doped silicon tips (Bruker, MESP-V2) with a nominal curvature radius of 20 nm. The tip lifted height was 100 nm, 200 nm and 300 nm. Data analysis was performed with the software Nanoscope Analysis 1.7.

2.6. Electrical characteristics test

The PEN film was first ultrasonically cleaned with absolute ethanol. Based on PEN, bottom platinum electrode with a thickness of 100 nm was prepared by magnetron sputter deposition. Next, *h*IAPP_{20–29} polypeptide fibrils was drop-cast on the bottom electrode. Finally, top silver electrode with a thickness of 80 nm was prepared by magnetron sputter deposition. Electrical characteristics of polypeptide fibrils were analyzed using Keithley 4200A SCS semiconductor system and Cascade Micromesh M150 probe station. During DC measurement, the Ag top electrode was connected to the applied voltage and the Pt bottom electrode was grounded. Suitable current limiter (CC) was used to prevent its breakdown.

2.7. Catalysis experiment

The reduction of 4-nitrophenol catalyzed by the gold nanoplates was carried out by following a previously reported procedure [31]. Typically, the Au-fibrils sediment after centrifugation was resuspended in 1 mL of Milli-Q water. Then, the suspension was mixed with 1 mL of 15 mM freshly prepared NaBH₄ aqueous solution and then placed undisturbed for 5 min. In the end, 1 mL of 4-nitrophenol solution with a concentration of 300 μ M was added into the above solution to initiate the reaction. The reaction was monitored at 400 nm via a UV-2600i spectrophotometer (Shimadzu, Japan) at 25 °C.

3. Results and discussion

3.1. Amyloid self-assembled fibrils and the electro-activity

The amyloid peptide hIAPP₂₀₋₂₉ plays a prominent role in the fibrillation of hIAPP₁₋₃₇ that is closely related to the pathogenesis of Type II diabetes. The mechanistic insight of self-assembling of this short peptide was well explored recently. The hetero zipper β -sheet has been identified as the main building unit of the fibrils [32]. Herein, we first investigated amyloid fibrillation of hIAPP₂₀₋₂₉ in Milli-Q water at three time points (0.5, 4, and 12 h) by atomic force microscopy (AFM). The average height of peptide oligomers (Fig. 1a) at 0.5 h was 2.4 nm, and it grew into short fibrils (Fig. 1b) with an average height of 9.6 nm at 4 h, and finally mature long fibrils were obtained with an average height of 51.6 nm at 12 h (Fig. 1c and 1f). Transmission electron microscope (TEM) images of hIAPP₂₀₋₂₉ oligomers, short fibrils and long fibrils corresponding to AFM images were also shown in Fig. S1. Thioflavin T (ThT) assay was used to monitor β -sheet structure formation during the fibrillation. It demonstrated that hIAPP₂₀₋₂₉ self-assembled stably as evidenced by the increase of ThT fluorescent signal, which approached the plateau after 480 min (Fig. 1d). The results suggest that the assembling of hIAPP₂₀₋₂₉ in Milli-Q water is a dynamic process. Subsequently, we further used circular dichroism (CD) spectroscopy to examine the

secondary structures of hIAPP₂₀₋₂₉ assemblies in Milli-Q water at three time points (0.5, 4, and 12 h). Consistent with the ThT assay, peptides presented a secondary structure conversion from random coil (0.5 h) to β -sheet (4 h and 12 h) (Fig. 1e).

Subsequently, the surface charge of hIAPP₂₀₋₂₉ fibrils was tested by electrostatic force microscope (EFM), which is a dual scanning technique (topographical profile as the first scan and phase profile as the second scan). The charges or dielectric constant on the surface of amyloid fibrils could be derived from the recorded information of phase images. Keeping applied voltage constant, the increment of lift height would lead to a depletion of phase shift signal (Φ) of hIAPP₂₀₋₂₉ fibrils. For instance, the phase shift was about 0.77, 0.33 and 0.18 degrees at lift height 100 nm, 200 nm and 300 nm, respectively (Fig. 2a and 2b). These results indicate that a large number of charges exist on the long fibrils surface, combined with zeta potential of hIAPP₂₀₋₂₉ amyloid fibrils in solution (Fig. S2), we could infer the positive charge existing on the fibril. The current–voltage (I – V) curve of hIAPP₂₀₋₂₉ fibrils metrix was tested, and the typical memristor I – V curve feature from the set-up device based hIAPP₂₀₋₂₉ amyloid fibrils as the active layer was obtained (Fig. 2c) with the current compliance (I_{cc}) set from 1 nA to 500 nA. The switching voltage was found to be independent of programming current, which almost maintained at 0.4 V with current compliance (I_{cc}) reduced to 1 nA. We proposed and set up a memristor device to test I – V curve because the memristive switching might be an electrochemical process related to an ionic/valence state change in the dielectric layer [33–35]. Therefore, Ag memristors was developed with hIAPP₂₀₋₂₉ fibrils and the verified memristive switching implied the electron or charge transfer along the amyloid fibrils, facilitating the electrochemical process of Ag⁺ to Ag. The molecular dynamic simulation of hIAPP₂₀₋₂₉ fibrils was performed and typical self-assembled filament of peptides was obtained (Fig. 2d). The surface polarity of peptide filament was also exhibited and positive and negative charge in blue and red color distributed on the surface of filament (Fig. 2e), which further consolidated EFM results above. Furthermore, the charge transfer could occur through-space n···n (O···O or N···O) and n··· π (N···C=O or O···C=O) interactions among the

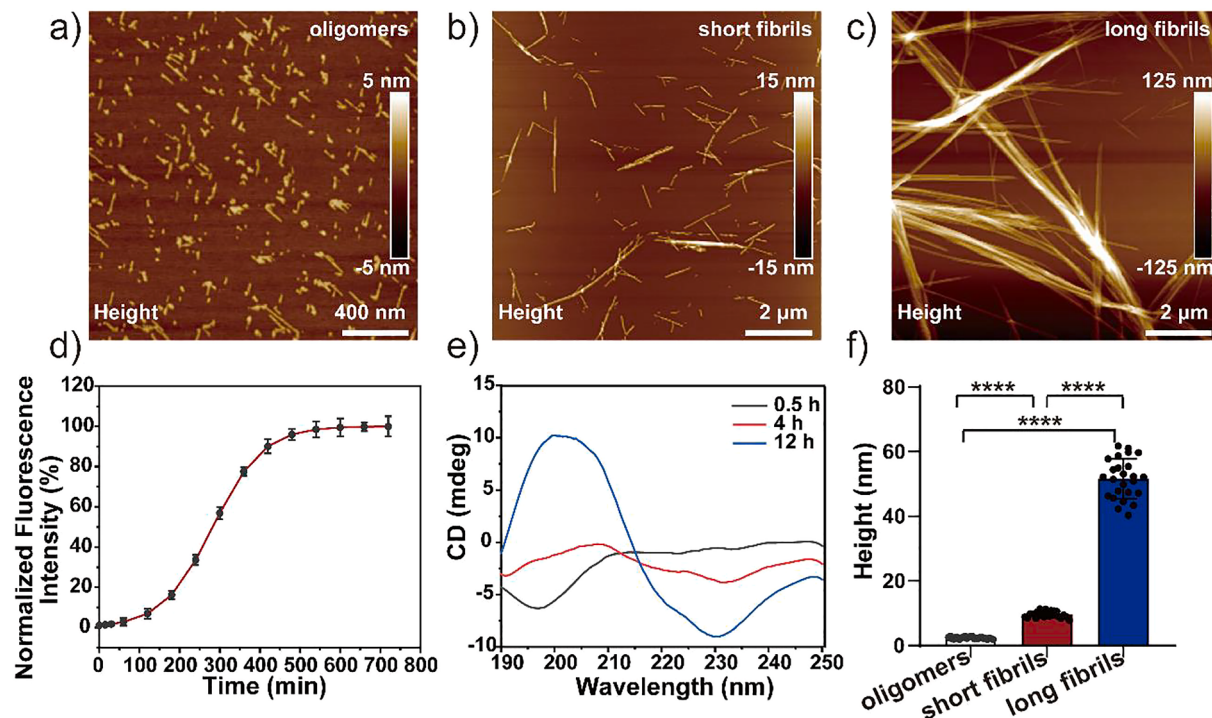


Fig. 1. Characterizations of the hIAPP₂₀₋₂₉ aggregates. (a, b, c) AFM images of hIAPP₂₀₋₂₉ oligomers, short fibrils and long fibrils. (d) ThT (thioflavin T) assay of hIAPP₂₀₋₂₉ in Milli-Q water. (e) Circular dichroism (CD) spectra of hIAPP₂₀₋₂₉ oligomers, short fibrils and long fibrils in Milli-Q water. (f) Height analysis of hIAPP₂₀₋₂₉ oligomers, short fibrils and long fibrils (one way analysis of variance (ANOVA) with Tukey's correction, ***P < 0.0001; error bars are s.d.).

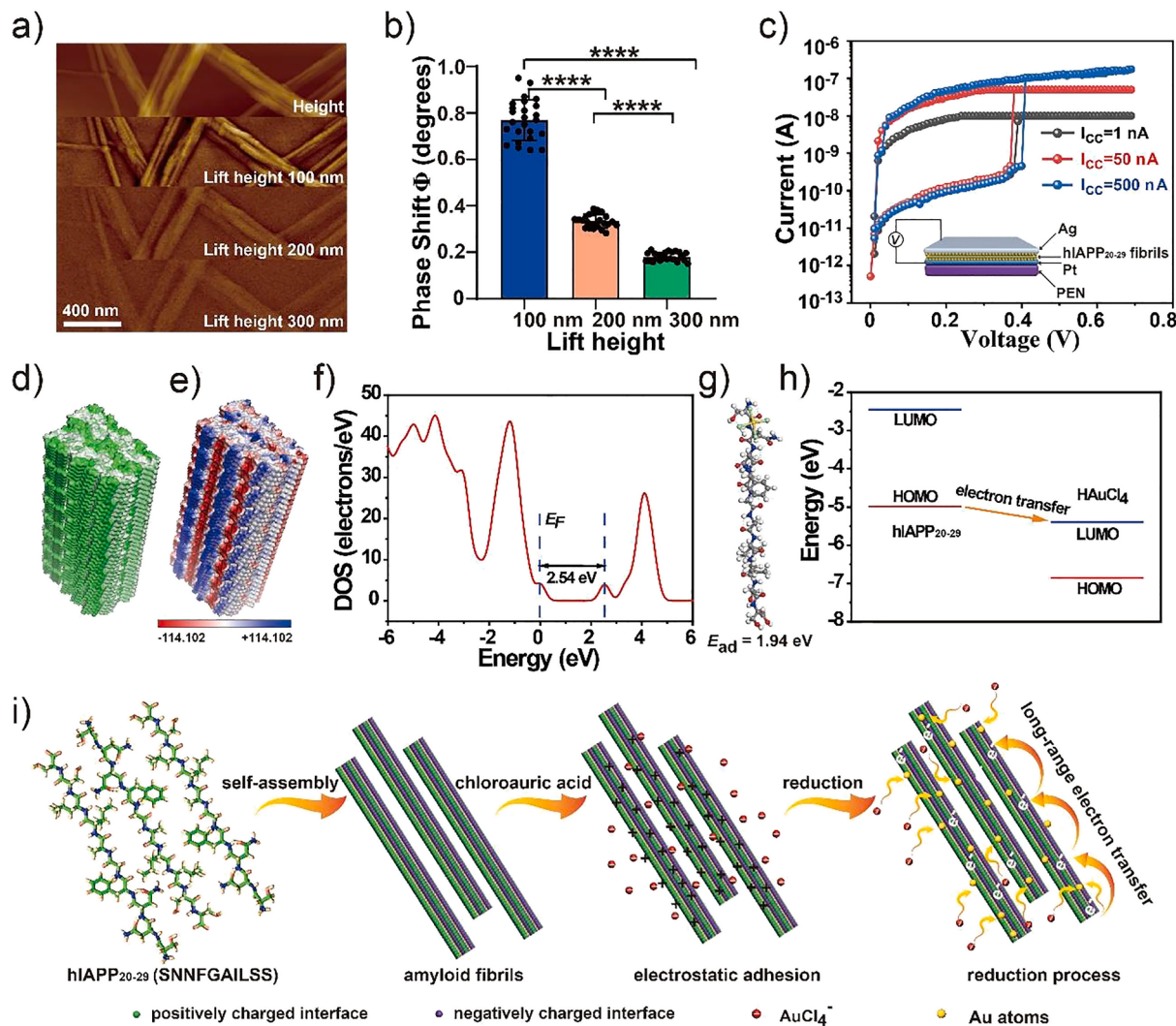


Fig. 2. Characterizations of hIAPP₂₀₋₂₉ long fibrils. (a) AFM height and EFM images of hIAPP₂₀₋₂₉ long fibrils. (b) Phase shifts at different lift height (one way analysis of variance (ANOVA) with Tukey's correction, ***P < 0.0001; error bars are s.d.). (c) Electrical characteristics of hIAPP₂₀₋₂₉ long fibrils. The inset is schematic of electron device composed of hIAPP₂₀₋₂₉ long fibrils (d) The distribution of hydrophobic core (white color) and hydrophilic interface (green color) in proto filament assembly of the hIAPP₂₀₋₂₉. (e) The distribution of positive charge (blue color) and negative charge interface (red color) on the hIAPP₂₀₋₂₉ filament. (f) Calculated DOS of the hIAPP₂₀₋₂₉. (g) Theoretical calculation of binding energy between hIAPP₂₀₋₂₉ and chloroauric acid. (h) Theoretical calculation of electron transfer between hIAPP₂₀₋₂₉ and chloroauric acid. (i) The schematic of amyloid peptide based fibrils with charge transportation facilitate the reduction of chloroauric acid. (For interpretation of the references to color in this figure legend, the reader is referred to the web version of this article.)

amino acids of peptides in the aggregative state, i.e., nanofibrils, which is consistent with points proposed by Tang [36]. The band gap of hIAPP₂₀₋₂₉ was further examined to be ~ 2.5 eV by calculating the density of states (DOS), which is the basis of charge transfer through peptides (Fig. 2f). After revealing the electroactive features of amyloid fibrils, we explored the possible mechanism of the amyloid peptide enabled synthesis of gold nanostructure by theoretical simulation (Fig. 2g and 2h). The binding energy between hIAPP₂₀₋₂₉ peptide and chloroauric acid was determined to be 1.94 eV at one binding site, and chloroauric acid could also bind to amyloid peptide at another three sites with binding energies of 1.81 eV, 1.87 eV and 1.73 eV (Fig. S3), which suggested that chloroauric acid could be enriched around the peptides to facilitate the subsequent redox reaction. The energy level distribution of hIAPP₂₀₋₂₉ and chloroauric acid further presented that the electron transfer occurs from the HOMO of the peptide to the LUMO of chloroauric acid. Taken together, we have proved the capability and possibility of hIAPP₂₀₋₂₉ peptides to facilitate the reduction of HAuCl₄ to the gold nanostructure mainly due to following points 1) the binding between the peptide and chloroauric acid, 2) electron transfer from the peptide to HAuCl₄, and 3)

charge transport along the surface of amyloid fibrils. The proposed schematic of self-assembled amyloid fibrils with charge transportation facilitating the reduction of HAuCl₄ was presented based on the results obtained (Fig. 2i), which clarified the mechanistic insight and structural requirement for peptide or peptide assemblies in the reduction process of metal ions.

3.2. Amyloid self-assembled fibrils facilitating the green synthesis of single-crystalline gold nanoplates

Next, hIAPP₂₀₋₂₉ fibrils were used as a biological reducing agent, dispersing agent and templates to synthesize gold nanostructures. hIAPP₂₀₋₂₉ mature fibrils solution was mixed with chloroauric acid aqueous solution and heated for 120 h without disturbance. Triangular and hexagonal two-dimensional gold nanoplates with different planar area were obtained at 25 °C, 37 °C and 60 °C (Fig. 3a and S4) after the products were washed in an alkaline solution to remove the fibrils. AFM and SEM images taken before the alkaline washing (Fig. S5) showed that the two-dimensional gold nanoplates were attached to the long fibrils,

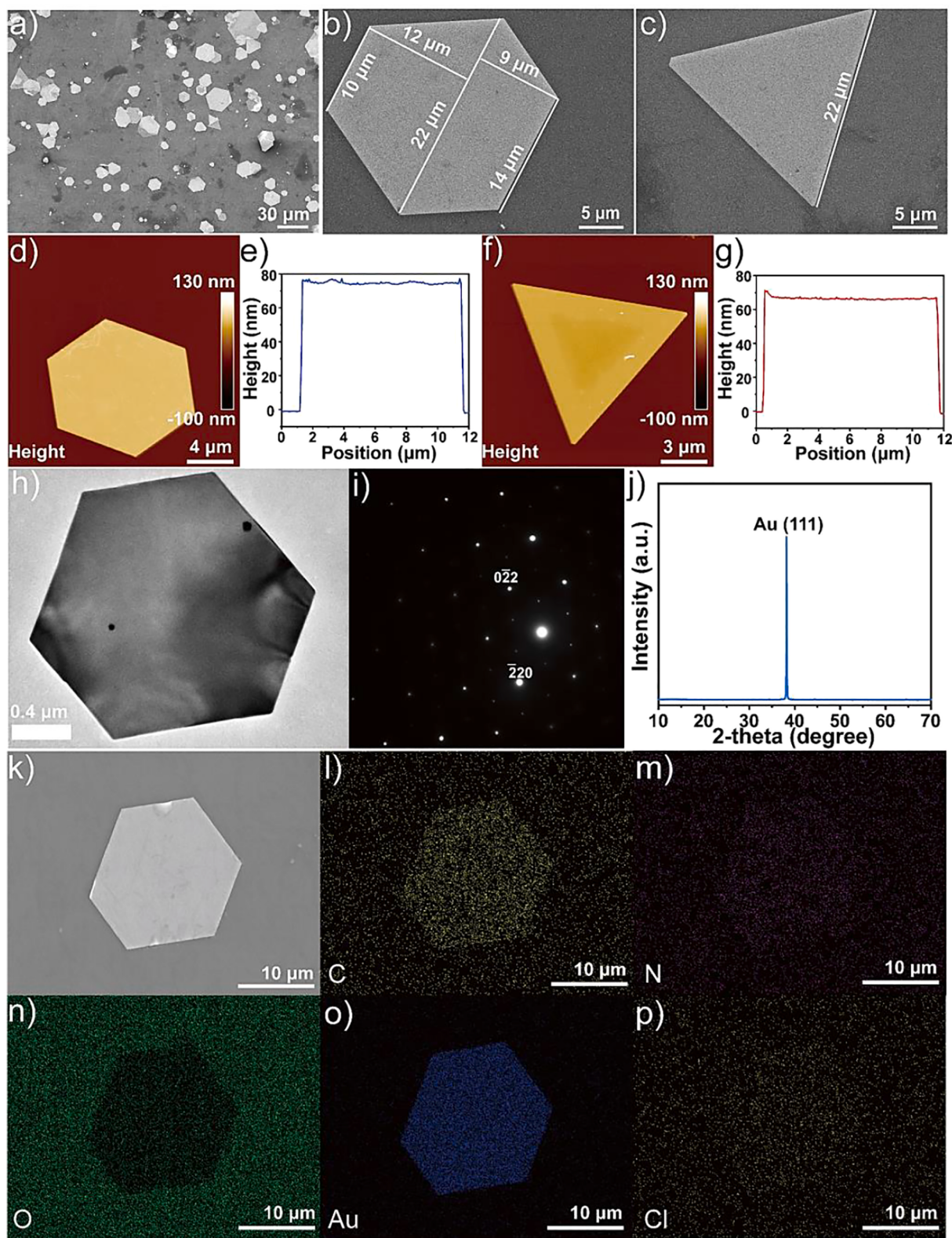


Fig. 3. Morphology characterization of the gold nanoplates. (a) Large area SEM image of two-dimensional gold nanoplates reduced by long fibrils. (b, c) SEM images of hexagonal and triangular gold nanoplates. (d, f) AFM images of hexagonal and triangular gold nanoplates. (e, g) Height analysis corresponding to (d, f), respectively. (h, i) TEM images of hexagonal gold nanoplates and the corresponding selected area electron diffraction pattern. (j) XRD data of hexagonal and triangular gold nanoplates on a silicon (Si) wafer substrate. (k-p) SEM image and elemental mapping (C, N, O, Au, Cl) of a hexagonal gold nanoplate.

forming the Au-fibrils hybrids. The planar area of the hexagonal and triangular two-dimensional gold nanoplates were determined to be $354 \mu\text{m}^2$ and $209 \mu\text{m}^2$, respectively. The thickness of the hexagonal flat gold nanoplate was measured to be about 75 nm, while the triangular gold nanoplate was perfectly flat with a constant height of 65 nm (Fig. 3b, 3c, and 3d-g). TEM images also demonstrated hexagonal and triangular two-dimensional gold nanoplates (Fig. 3h and S6a). Selected area electron diffraction (SAED) of the hexagonal gold nanoplate (Fig. 3i) showed six diffraction spots with six-fold symmetry, which is in agreement with the face-centered cubic (f.c.c) structure of gold and the flat surface of the gold nanoplate. The second strongest intensity set of diffraction spots were in accordance with the (2_0) planes of (f.c.c) gold structure. Furthermore, the XRD spectrum (the XRD spectrum (Fig. 3j)) exhibited a single (1 1 1) peak along the full scanning angle range, indicating that the nanoplate is single-crystalline. The multilayered structure of gold nanoplates was demonstrated by AFM (Fig. S7), which reveals the characteristic of preferential planar crystal growth. The energy dispersive X-ray spectroscopy mapping characterization of the nanoplates showed that Au and C were distributed over the whole area of the

nanoplates (Fig. 3k-3p and S8).

Furthermore, we examined the role of specific amino acids of hIAPP₂₀₋₂₉ (i.e. F, N, S) in mediating the synthesis of gold nanoplates (Fig. S9), and it was found that the examined amino acids rarely exhibited the capability of reducing chloroauric acid to the gold nanostructure. The mutation of hIAPP₂₀₋₂₉ in which N, N, and F mutated with G also weakened the ability of reducing HAuCl₄ to the gold nanoplates (Fig. S10). In addition, two-dimensional gold nanoplates were still obtained via the same reduction of chloroauric acid by hIAPP₂₀₋₂₉ fibrils, although with isopropyl alcohol (IPA) as hydroxyl radical scavengers, however amorphous gold nanostructures were obtained in the presence of ethylenediaminetetraacetic acid (EDTA) as hole scavengers (Fig. S11). The electron and hole existed and involved in the reduction of chloroauric acid by hIAPP₂₀₋₂₉ fibrils, and in our test, if the hole could be depleted by EDTA in the system, it could lead to the interruption of synthesis of gold nanoplates, which further verified the key role of charge transportation in the reduction. The results obtained above suggests that the wild type amyloid peptide hIAPP₂₀₋₂₉ fibrils with highly ordered structure and long-range charge transport as the

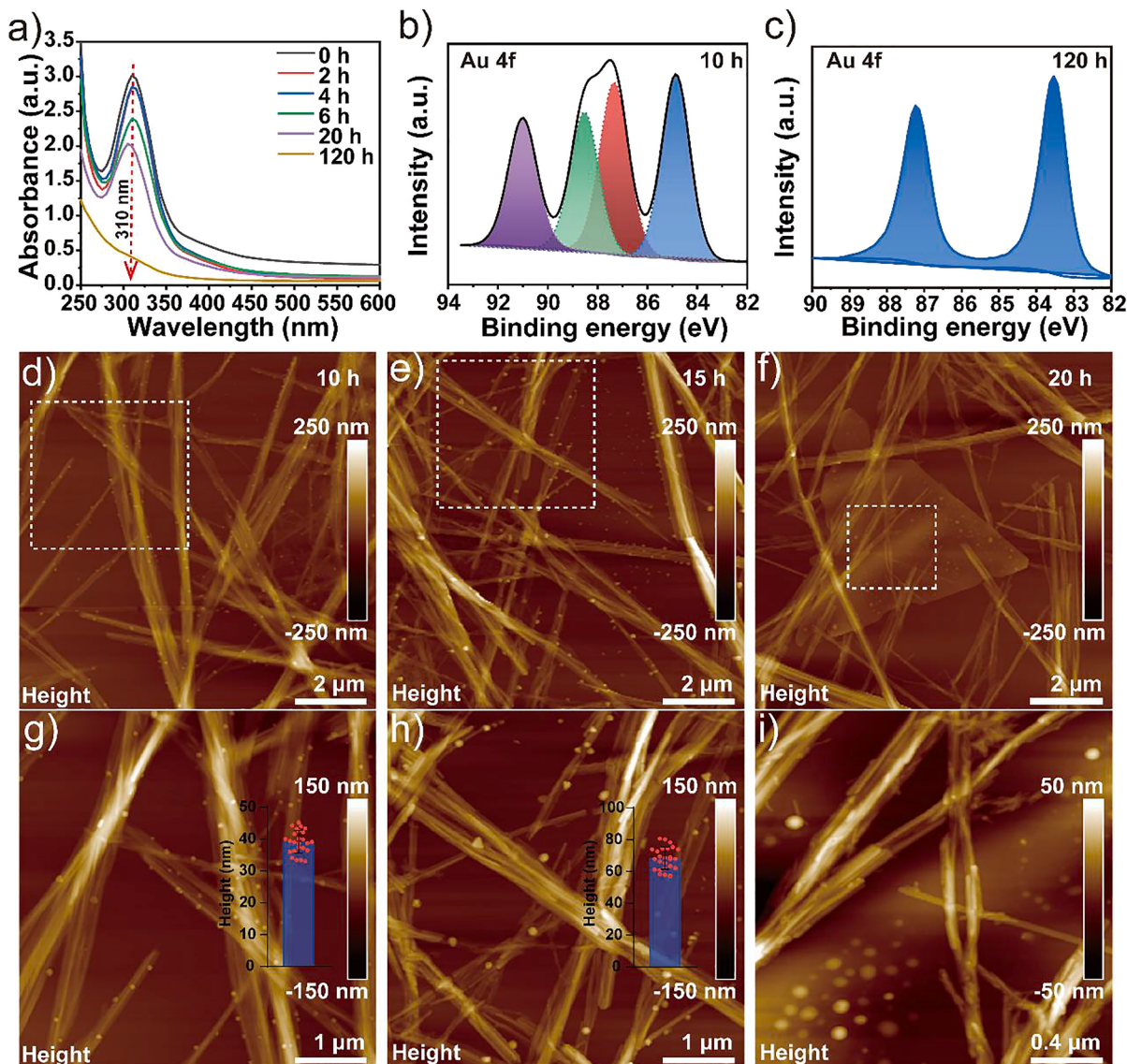


Fig. 4. Kinetics of the synthesis of gold nanoplates. (a) UV-vis absorption spectra of the reaction of chloroauric acid and hIAPP₂₀₋₂₉ long fibrils. (b, c) XPS spectra taken from gold nanoplates reduced by hIAPP₂₀₋₂₉ long fibrils with 10 h and 120 h reaction time, respectively. (d, e, f) AFM images of the reaction process of chloroauric acid and hIAPP₂₀₋₂₉ long fibrils, 10 h, 15 h and 20 h reaction time, respectively. (g, h, i) Partial high-resolution images corresponding to selected area of (d, e, f), respectively. The inserts in (g, h) are the height statistics of gold nanostructures.

template could present the superiority in facilitating the green synthesis of 2D single crystal gold nanoplates.

To understand the kinetics of the green synthesis of 2D gold nanoplates, continuous UV-vis spectra was measured to monitor the reaction. The characteristic absorption peak assigned to chloroauric acid at 310 nm gradually decreased, but the UV-vis spectrum of sample did not show any peak of surface plasmon resonance (SPR) of gold nanostructure during the 120 h reaction (Fig. 4a). It indicates that the chloroauric acid is slowly reduced by hiAPP₂₀₋₂₉ fibrils, and the whole reaction process is relatively mild, but crystal growth might be fast. To further investigate the chloroauric acid changes induced by hiAPP₂₀₋₂₉ fibrils, X-ray photoelectron spectroscopy (XPS) was utilized to monitor kinetic synthetic procedure that is represented by the binding energy of Au element. According to the survey spectrum, obvious peak of Au 4f can be observed, which proved that the AuCl₄⁻ ions were reduced to the zero valence state (Fig. S12). After more specific analysis, the sharp peaks at 91.10 eV, 88.50 eV, 87.38 eV and 84.70 eV corresponded to AuCl₄⁻, AuCl and Au, which suggested the chloroauric acid in the sample was reduced and the reduction proceeded gradually during 10-hour reaction (Fig. 4b). However, zero valence state (Au⁰) at 87.38 eV and 83.88 eV in the sample was detected until the reaction lasted for 120 h (Fig. 4c), which implied that the reduction reaction of chloroauric acid was completed, and UV-vis absorption spectrum also verified it.

In addition, AFM was used to map the morphology evolution of the gold nanostructure reduced by hiAPP₂₀₋₂₉ fibrils. We captured the gold nanoparticles with the height of about 39.16 nm attached to the surface of the amyloid fibrils after 10-hour reaction (Fig. 4d and 4 g), and they grew into small triangular two-dimensional gold nanoplates with the height of about 68.41 nm (Fig. 4e and 4 h), and finally larger 2D nanoplates were obtained (Fig. 4f and 4 i). In summary, the comprehensive analysis of the results obtained above clarified that AuCl₄⁻ could adsorb onto the surface of hiAPP₂₀₋₂₉ fibrils and be gradually reduced to gold atoms, which nucleate and assemble along the (111) facet and finally grow into 2D single-crystalline gold nanostructures with triangular and hexagonal shapes.

3.3. Reduction of 4-nitrophenol by Au-fibrils hybrids

To explore the applications of the Au-fibrils hybrids, we used the material as a hydrogen transfer catalyst in the reduction of 4-nitrophenol by sodium borohydride. As shown in Fig. 5a, active hydrogen on the gold surface was provided by sodium borohydride in the solution, and it reacted with 4-nitrophenol to produce the unstable intermediate

4-nitrosophenol, 4-hydroxyaminophenol and finally 4-aminophenol [31]. The catalytic reaction was performed in Milli-Q water at 25 °C with the initial 4-nitrophenol concentration of 100 μM. The effect of the concentration and the morphology of catalyst on the reaction efficiency was evaluated by monitoring the UV-vis spectra of 4-nitrophenol (Fig. 5b and 5d, S13). As the reaction continued, the intensity at 400 nm gradually decreased, while the intensity at 310 nm increased, indicating that 4-nitrophenol was constantly consumed and 4-aminophenol was the dominated product. The conversion of 4-nitrophenol was found to be in a positive correlation to the Au concentration of Au-fibrils hybrids, and the conversion increased with the extension of the reaction time. With 300 μM of Au (Au-fibrils hyrids), a conversion efficiency of 95.1% was achieved in 7 min (Fig. 5c). As the concentration of Au decreased (150 μM, 75 μM, 35 μM, 15 μM), longer time was needed to complete the reduction (Fig. S14a-d). A conversion efficiency of 58.9 % was achieved with only 5 μM of Au (Fig. 5e). However, when the concentration of catalyst was decreased to 3 μM, the reduction of 4-nitrophenol did not proceed (Fig. S14e). As a comparison, 2D gold nanoplates after alkaline washing could hardly catalyze the reduction of 4-nitrophenol, possibly due to the lack of peptide component (Fig. S13a). Likewise, gold nanoparticles obtained by sodium borohydride reduction of chloroauric acid could not catalyze this reduction either (Fig. S13b). To sum up, Au-fibrils hybrids could be used as a green catalyst for the conversion of 4-nitrophenol to 4-aminophenol with a low catalyst concentration at room temperature with superior performance, which is also attributed to the electroactive feature of hiAPP₂₀₋₂₉ fibrils [37].

4. Conclusions

In summary, we revealed the electroactivity of hiAPP₂₀₋₂₉ peptide and its self-assembled amyloid fibrils, exhibiting the charge transport along the surface of fibrils. Meanwhile, they could bind to chloroauric acid and make the electron transfer in between. All these features endow the hiAPP₂₀₋₂₉ fibrils with possibility and capability to facilitate the reduction of HAUCl₄ to the gold nanostructures in an eco-friendly manner as the capping and reducing agents. Furthermore, the obtained Au-fibrils hybrids have been explored as a green catalyst in an efficient and rapid reduction of 4-nitrophenol. We envision that the proposed electro-active amyloid fibrils could be applied to construct a variety of peptide-metal nanomaterials in a green and precise manner and further be applied in a diversity of applications, such as catalysis, biosensing and bioimaging, etc.

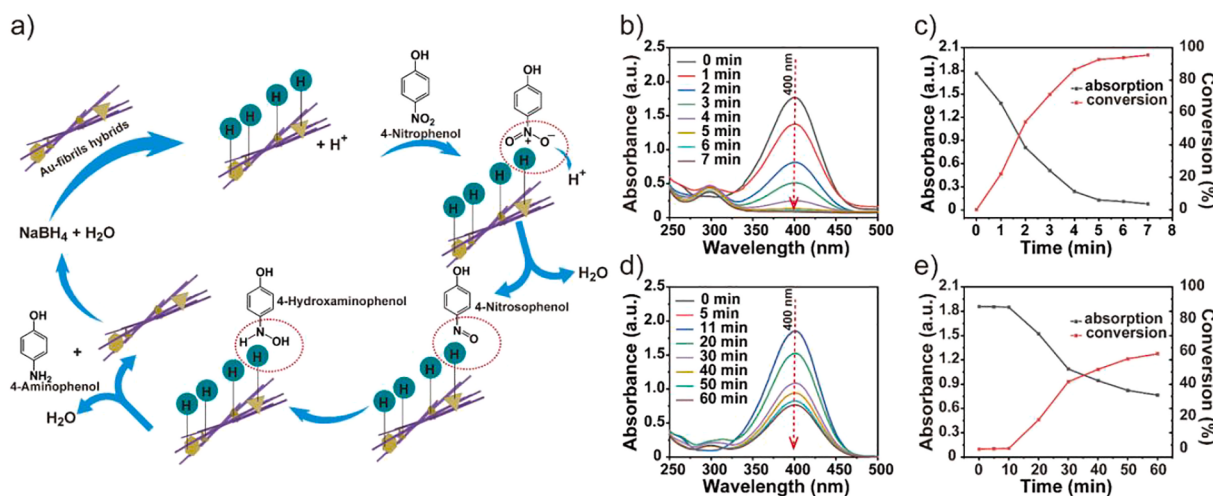


Fig. 5. (a) Visual illustration of reduction of 4-nitrophenol catalyzed by the Au-fibrils hybrids. (b, d) UV-vis absorption spectra of 4-nitrophenol decreases over time. (c, e) Variation of the intensity of peak at 400 nm, conversions of 4-nitrophenol catalyzed by the Au-fibrils hybrids at different times. Reaction conditions: reaction temperature, 25 °C; 4-nitrophenol concentration, 100 μM; Au concentration, 300 μM (b, c) and 5 μM (d, e), respectively.

Data availability

All data are available in the main text or the [supplementary materials](#).

Author contribution

Liwei Zhang: Conceptualization, Methodology, Formal analysis, Data curation, Writing – original draft, Writing – review & editing. **Peng Zhang:** Software, Formal analysis. **Rongrong Wu:** Software. **Aoze Han:** Methodology, Formal analysis, Data curation. **Kai Cheng:** Formal analysis, Data curation. **Zengkai Wang:** Formal analysis, Data curation. **Juan Yang, Shuai Hou, Yi Tong and Mingdong Dong:** Writing – review & editing. **Lei Liu:** Writing – review & editing, Supervision, Funding acquisition. All authors read and commented on the manuscript.

Declaration of Competing Interest

The authors declare that they have no known competing financial interests or personal relationships that could have appeared to influence the work reported in this paper.

Data availability

Data will be made available on request.

Acknowledgements

We greatly acknowledge the financial support from the National Natural Science Foundation of China (22072060, 21573097).

Appendix A. Supplementary material

Supplementary data to this article can be found online at <https://doi.org/10.1016/j.apsusc.2023.156937>.

References

- [1] Y. Choi, S.Y. Lee, Biosynthesis of inorganic nanomaterials using microbial cells and bacteriophages, *Nat. Rev. Chem.* 4 (2020) 638–656.
- [2] J. Zhou, Y. Yang, C.-Y. Zhang, Toward biocompatible semiconductor quantum dots: from biosynthesis and bioconjugation to biomedical application, *Chem. Rev.* 115 (2015) 11669–11717.
- [3] K.B. Narayanan, N. Sakhivel, Biological synthesis of metal nanoparticles by microbes, *Adv. Colloid Interface Sci.* 156 (2010) 1–13.
- [4] P. Mohanpuri, N.K. Rana, S.K. Yadav, Biosynthesis of nanoparticles: technological concepts and future applications, *J. Nanopart. Res.* 10 (2008) 507–517.
- [5] R. Cui, H.-H. Liu, H.-Y. Xie, Z.-L. Zhang, Y.-R. Yang, D.-W. Pang, Z.-X. Xie, B.-B. Chen, B. Hu, P. Shen, Living yeast cells as a controllable biosynthesizer for fluorescent quantum dots, *Adv. Funct. Mater.* 19 (2009) 2359–2364.
- [6] J. Xie, Y. Zheng, J.Y. Ying, Protein-directed synthesis of highly fluorescent gold nanoclusters, *J. Am. Chem. Soc.* 131 (2009) 888–889.
- [7] Y.N. Tan, J.Y. Lee, D.I.C. Wang, Uncovering the design rules for peptide synthesis of metal nanoparticles, *J. Am. Chem. Soc.* 132 (2010) 5677–5686.
- [8] L. Leon, W. Su, H. Matsui, R. Tu, Interfacial templating of inorganic nanostructures using a growth directing and reducing peptide, *Soft Matter* 7 (2011) 10285–10290.
- [9] J. Zhou, A. Saha, J. Adamcik, H. Hu, Q. Kong, C. Li, R. Mezzenga, Macroscopic single-crystal gold microflakes and their devices, *Adv. Mater.* 27 (2015) 1945–1950.
- [10] S. Bolisetty, J.J. Vallooran, J. Adamcik, S. Handschin, F. Gramm, R. Mezzenga, Amyloid-mediated synthesis of giant, fluorescent, gold single crystals and their hybrid sandwiched composites driven by liquid crystalline interactions, *J. Colloid Interface Sci.* 361 (2011) 90–96.
- [11] L. Lv, X. Wu, Y. Yang, X. Han, R. Mezzenga, C. Li, Trans-scale 2D synthesis of millimeter-large au single crystals via silk fibroin templates, *ACS Sustain. Chem. Eng.* 6 (2018) 12419–12425.
- [12] H. Lee, H.-S. Jang, D.-H. Cho, J. Lee, B. Seong, G. Kang, Y.-S. Park, K.T. Nam, Y.-S. Lee, D. Byun, Redox-active tyrosine-mediated peptide template for large-scale single-crystalline two-dimensional silver nanosheets, *ACS Nano* 14 (2020) 1738–1744.
- [13] M.B. Dickerson, K.H. Sandhage, R.R. Naik, Protein- and peptide-directed syntheses of inorganic materials, *Chem. Rev.* 108 (2008) 4935–4978.
- [14] M. Li, X. Wu, J. Zhou, Q. Kong, C. Li, Single-crystal Au microflakes modulated by amino acids and their sensing and catalytic properties, *J. Colloid Interface Sci.* 467 (2016) 115–120.
- [15] Y. Tan, R.Y. Adhikari, N.S. Malvankar, S. Pi, J.E. Ward, T.L. Woodard, K.P. Nevin, Q. Xia, M.T. Tuominen, D.R. Lovley, Synthetic biological protein nanowires with high conductivity, *Small* 12 (2016) 4481–4485.
- [16] D.M. Shapiro, G. Mandava, S.E. Yalcin, P. Arranz-Gibert, P.J. Dahl, C. Shipps, Y. Gu, V. Srikanth, A.I. Salazar-Morales, J.P. O'Brien, K. Vanderschuren, D. Vu, V. S. Batista, N.S. Malvankar, F.J. Isaacs, Protein nanowires with tunable functionality and programmable self-assembly using sequence-controlled synthesis, *Nat. Commun.* 13 (2022) 829.
- [17] C. Ma, J. Dong, M. Viviani, I. Tulini, N. Pontillo, S. Maity, Y. Zhou, W.H. Roos, K. Liu, A. Herrmann, G. Portale, De novo rational design of a freestanding, supercharged polypeptide, proton-conducting membrane, *Sci. Adv.*, 6 (2020) eabc0810.
- [18] J. O'Donnell, P.-A. Cazade, S. Guerin, A. Djeghaber, E.U. Haq, K. Tao, E. Gazit, E. Fukada, C. Silien, T. Soulimane, D. Thompson, S.A.M. Tofail, Piezoelectricity of the Transmembrane protein ba3 cytochrome c oxidase, *Adv. Funct. Mater.* 31 (2021) 2100884.
- [19] N. Amdursky, D. Marchak, L. Sepunaru, I. Pecht, M. Sheves, D. Cahen, Electronic transport via proteins, *Adv. Mater.* 26 (2014) 7142–7161.
- [20] P. Hammarström, Photonic amyloids, *Nat. Photon.* 13 (2019) 442–444.
- [21] K. Tao, P. Makam, R. Aizen, E. Gazit, Self-assembling peptide semiconductors, *Science*, 358 (2017) eaam9756.
- [22] K. Tao, Z. Fan, L. Sun, P. Makam, Z. Tian, M. Ruegsegger, S. Shaham-Niv, D. Hansford, R. Aizen, Z. Pan, S. Galster, J. Ma, F. Yuan, M. Si, S. Qu, M. Zhang, E. Gazit, J. Li, Quantum confined peptide assemblies with tunable visible to near-infrared spectral range, *Nat. Commun.* 9 (2018) 3217.
- [23] B. Sun, K. Tao, Y. Jia, X. Yan, Q. Zou, E. Gazit, J. Li, Photoactive properties of supramolecular assembled short peptides, *Chem. Soc. Rev.* 48 (2019) 4387–4400.
- [24] J. Pansieri, V. Josserand, S.-J. Lee, A. Rongier, D. Imbert, M.M. Sallanon, E. Kóvari, T.G. Dane, C. Vendrel, O. Chaix-Pluchery, M. Guidetti, J. Vollaire, A. Fertin, Y. Usson, P. Rannou, J.-L. Coll, C. Marquette, V. Forge, Ultraviolet-visible–near-infrared optical properties of amyloid fibrils shed light on amyloidogenesis, *Nat. Photon.* 13 (2019) 473–479.
- [25] K. Tao, B. Xue, D. Chovan, N. Brown, L.J.W. Shimon, O. Maraba, Y. Cao, S. A.M. Tofail, D. Thompson, J. Li, R. Yang, E. Gazit, Bioinspired stable and photoluminescent assemblies for power generation, *Adv. Mater.* 31 (2019) 1807481.
- [26] K. Tao, B. Xue, Q. Li, W. Hu, L.J.W. Shimon, P. Makam, M. Si, X. Yan, M. Zhang, Y. Cao, R. Yang, J. Li, E. Gazit, Stable and optoelectronic dipeptide assemblies for power harvesting, *Mater. Today* 30 (2019) 10–16.
- [27] H. Yuan, P. Han, K. Tao, S. Liu, E. Gazit, R. Yang, Piezoelectric peptide and metabolite materials, *Research* 2019 (2019) 9025939.
- [28] P. Chakraborty, H. Oved, D. Bychenko, Y. Yao, Y. Tang, S. Zilberman-Tal, G. Wei, T. Dvir, E. Gazit, Nanoengineered peptide-based antimicrobial conductive supramolecular biomaterial for cardiac tissue engineering, *Adv. Mater.* 33 (2021) 2008715.
- [29] S. Bera, S. Guerin, H. Yuan, J. O'Donnell, N.P. Reynolds, O. Maraba, W. Ji, L.J. W. Shimon, P.-A. Cazade, S.A.M. Tofail, D. Thompson, R. Yang, E. Gazit, Molecular engineering of piezoelectricity in collagen-mimicking peptide assemblies, *Nat. Commun.* 12 (2021) 2634.
- [30] V. Basavalingappa, S. Bera, B. Xue, J. O'Donnell, S. Guerin, P.-A. Cazade, H. Yuan, E.u. Haq, C. Silien, K. Tao, L.J.W. Shimon, S.A.M. Tofail, D. Thompson, S. Kolusheva, R. Yang, Y. Cao, E. Gazit, Diphenylalanine-Derivative Peptide Assemblies with Increased Aromaticity Exhibit Metal-like Rigidity and High Piezoelectricity, *ACS Nano*, 14 (2020) 7025–7037.
- [31] Y. Feng, H. Wang, J. Zhang, Y. Song, M. Meng, J. Mi, H. Yin, L. Liu, Bioinspired synthesis of Au nanostructures templated from amyloid β peptide assembly with enhanced catalytic activity, *Biomacromolecules* 19 (2018) 2432–2442.
- [32] Y. Song, B. Dai, Y. Wang, Y. Wang, C. Liu, P. Gourdon, L. Liu, K. Wang, M. Dong, Identifying hetero zipper β -sheet in twisted amyloid aggregation, *Nano Lett.* 22 (2022) 3707–3712.
- [33] X. Xu, X. Zhou, T. Wang, X. Shi, Y. Liu, Y. Zuo, L. Xu, M. Wang, X. Hu, X. Yang, J. Chen, X. Yang, L. Chen, P. Chen, H. Peng, Robust DNA-bridged memristor for textile chips, *Angew. Chem. Int. Ed.* 59 (2020) 12762–12768.
- [34] T. Fu, X. Liu, H. Gao, J.E. Ward, X. Liu, B. Yin, Z. Wang, Y. Zhuo, D.J.F. Walker, J. Joshua Yang, J. Chen, D.R. Lovley, J. Yao, Bioinspired bio-voltage memristors, *Nat. Commun.*, 11 (2020) 1861.
- [35] M.-K. Song, S.D. Namgung, D. Choi, H. Kim, H. Seo, M. Ju, Y.H. Lee, T. Sung, Y.-S. Lee, K.T. Nam, J.-Y. Kwon, Proton-enabled activation of peptide materials for biological bimodal memory, *Nat. Commun.* 11 (2020) 5896.
- [36] H. Zhang, B.Z. Tang, Through-space interactions in clusteroluminescence, *JACS Au* 1 (2021) 1805–1814.
- [37] T. Sun, Y. Feng, J. Peng, Y. Hao, L. Zhang, L. Liu, Cofactors-like peptide self-assembly exhibiting the enhanced catalytic activity in the peptide-metal nanocatalysts, *J. Colloid Interface Sci.* 617 (2022) 511–524.